5. A. Ourmazd, J. C. H. Spence, *Nature* **329**, 425 (1987).
6. N. P. Huxford, D. J. Eaglesham, C. J. Humphreys, *Nature* **329**, 812 (1987).
7. Y. Yan, M. G. Blanchin, *Phys. Rev.* **43**, 13717 (1991).
8. T. Krekels, G. Van Tendeloo, S. Amelinckx, *Appl. Phys. Lett.* **59**, 3048 (1991).
9. G. Van Tendeloo, T. Krekels, in *Characterization of High T_C Materials and Devices by Electron Microscopy*, N. D. Browning, S. J. Pennycook, Eds. (Cambridge Univ. Press, Cambridge, 2000), pp. 161–191.
10. W. Coene, G. Janssen, M. Op de Beeck, D. Van Dyck, *Phys. Rev. Lett.* **69**, 3743 (1992).
11. C. L. Jia, A. Thust, *Phys. Rev. Lett.* **82**, 5052 (1999).
12. S. Horiuchi et al., *Ultramicroscopy* **39**, 231 (1991).
13. S. J. Pennycook, D. E. Jesson, P. D. Nellist, M. F. Chisholm, N. D. Browning, in *Handbook of Microscopy*, S. Amelinckx et al., Eds. (Wiley-VCH, Weinheim, Germany, 1997), vol. 2, pp. 595–620.
14. P. M. Voyles, D. A. Muller, J. L. Grazul, P. H. Citrin, H. J. L. Gossmann, *Nature* **416**, 826 (2002).
15. P. E. Batson, N. Dellby, O. L. Krivanek, *Nature* **418**, 617 (2002).
16. A. Ohtomo, D. A. Muller, J. L. Grazul, H. Y. Hwang, *Nature* **419**, 378 (2002).
17. M. Haider et al., *Nature* **392**, 768 (1998).
18. M. Lentzen et al., *Ultramicroscopy* **92**, 233 (2002).
19. J. C. H. Spence, *Experimental High-Resolution Electron Microscopy* (Oxford Univ. Press, New York, 1988).
20. D. B. Williams, C. B. Carter, *Transmission Electron Microscopy* (Plenum, New York, 1996).
21. R. Kilaas, in *Proceedings of the 45th Annual Meeting of the Electron Microscopy Society of America*, Baltimore, MD, G. W. Bailey, Ed. (San Francisco Press, San Francisco, 1987), pp. 66–67.
22. All experimental images presented are prints obtained from the original and unfiltered digital CCD camera recordings.
23. Intensity traces were taken from the nonprocessed, original digital data.
24. H. W. Zandbergen, R. Gronsky, K. Wang, G. Thomas, *Nature* **331**, 596 (1988).
25. D. E. Morris et al., *Phys. Rev. B* **40**, 11406 (1989).

Formation of Electron Holes and Particle Energization During Magnetic Reconnection

J. F. Drake,[1]* M. Swisdak,[1] C. Cattell,[2] M. A. Shay,[1]
B. N. Rogers,[3] A. Zeiler[4]

Three-dimensional particle simulations of magnetic reconnection reveal the development of turbulence driven by intense electron beams that form near the magnetic x-line and separatrices. The turbulence collapses into localized three-dimensional nonlinear structures in which the electron density is depleted. The predicted structure of these electron holes compares favorably with satellite observations at Earth's magnetopause. The birth and death of these electron holes and their associated intense electric fields lead to strong electron scattering and energization, whose understanding is critical to explaining why magnetic explosions in space release energy so quickly and produce such a large number of energetic electrons.

Magnetic reconnection is the driver of explosions in laboratory, space, and astrophysical plasmas, including solar and stellar flares and storms in Earth's magnetosphere. In the classic picture of magnetic reconnection, oppositely directed components of the magnetic field cross-link, forming a magnetic x-line configuration. The expansion of the newly reconnected field lines away from the x-line releases the magnetic energy and pulls in the oppositely directed magnetic flux to sustain the energy release process. Some form of dissipation is required to allow the plasma and magnetic field to decouple so that the topological change in the magnetic field can take place. The rate of reconnection, however, is sensitive to the plasma resistivity (*1–3*) such that reconnection based on classical resistivity is orders of magnitude too slow to explain the fast release of magnetic energy observed in nature. To explain the large discrepancy between observations of energy release times and the predictions, it was postulated that the plasma resistivity is enhanced above the classical values by electron scattering associated with electric field fluctuations (*4*). These fluctuations could be driven by the intense currents that form during magnetic reconnection. The resulting anomalous resistivity fortuitously also facilitates fast reconnection, which is insensitive to resistivity (*5, 6*).

The concept of anomalous resistivity also has a secondary benefit. Observations of solar flares indicate that up to half of the energy released in magnetic reconnection is carried by energetic electrons (*7*). The direct production of very energetic electrons during magnetic reconnection in Earth's magnetotail has also been reported (*8*). The mechanism for such strong electron heating remains unclear. The flows that develop during reconnection are typically of the order of the Alfvén speed $c_A = B/[(4\pi\rho)^{1/2}]$, where B is the magnetic field strength and ρ is the plasma mass density, and are therefore too slow to produce the near relativistic electron velocities observed. The development of high-frequency turbulence, which could cause the electron scattering associated with anomalous resistivity, would also heat electrons and perhaps produce the broad spectrum of energetic electrons observed in nature.

Anomalous resistivity has been widely invoked to explain the fast release of energy observed in nature, but the concept remains poorly understood (*4*). The strongest evidence for its existence comes from observations in the auroral region of the ionosphere, where localized regions of large parallel electric field have been measured (*9, 10*). These localized structures take the form of double layers (which support a net drop in the electric potential) or electron holes (regions of depressed electron density that exhibit a bipolar parallel electric field).

We carried out three-dimensional (3D) particle simulations of magnetic reconnection to explore the self-consistent development of current-driven instabilities and anomalous resistivity and compared the results with observations from the Polar spacecraft at Earth's magnetopause. In earlier simulations of a system with a reversed field and no imposed ambient guide (out-of-plane) magnetic field, no current-driven instabilities developed around the x-line (*11*). The intrinsic electron heating around the null field region was sufficient to stabilize current-driven instabilities. In our simulations, an imposed guide field prevents the demagnetization of electrons and associated heating. The initial equilibrium is a double current layer with two magnetic field components B_x and B_z dependent on the spatial coordinate y:

$$\frac{B_x}{B_0} = \tanh\frac{y - L_y/4}{w_0} - \tanh\frac{y - 3L_y/4}{w_0} - 1 \quad (1)$$

where B_0 is the asymptotic field strength outside of the current layers; $B_z = (B^2 - B_x^2)^{1/2}$ is chosen so that the total field B is constant. For the 3D simulations shown, the computational domain has dimensions $L_x = 4d_i$, $L_y = 2d_i$, $L_z = d_i$ and periodic boundary conditions. The scale length d_i is the ion inertial length c/ω_{pi}, where ω_{pj} is the plasma frequency of a particle species j, and $w_0 = 0.25d_i$ is the current layer thickness. The initial plasma pressure is constant with the density n_0 and electron and ion temperatures $T_e = T_i = 0.04\ m_i c_A^2$, where $c_A = B_0/[(4\pi\ n_0 m_i)^{1/2}]$. Other parameters are B

[1]University of Maryland, College Park, MD 20742, USA. [2]School of Physics and Astronomy, University of Minnesota, Minneapolis, MN 55455, USA. [3]Department of Physics and Astronomy, Dartmouth College, Hanover, NH 03755, USA. [4]Centre for Interdisciplinary Plasma Science, Max-Planck-Institut für Plasmaphysik, 85748 Garching, Germany.

*To whom correspondence should be addressed. E-mail: drake@plasma.umd.edu

$= 26^{1/2}B_0$, the ion to electron mass ratio $m_i/m_e = 100$, and the velocity of light $c = 20c_A$. The electromagnetic field data are defined on a grid of $(N_x, N_y, N_z) = (512, 256, 128)$ points with an average of 40 particles per grid cell. To highlight the role of turbulence in the simulation, we later discuss data from a 2D simulation ($N_z = 1$) with otherwise identical parameters.

At a time $t = 3.4\ \Omega_{ci}^{-1}$ into the 3D simulation, with $\Omega_{ci} = eB_0/m_ic$ the ion cyclotron frequency, reconnection has driven a strong magnetic-field-aligned current near the x-line at $x/d_i = 1.0$ (Fig. 1, A and B). This current is dominantly carried by the electrons. Consistent with recent kinetic models, the magnetic field is an open x-line configuration (i.e., the separatrices intersect at a finite angle) that leads to fast reconnection (Fig. 1A). In 2D simulations the reconnection rate is comparable. However, in 3D the current layer becomes turbulent (movie S1) and the electrons are much more strongly heated in comparison to 2D.

The initial current layer is weakly unstable to the Buneman instability (12), which is driven by the relative drift of electrons and ions. In the initial state the peak electron drift speed v_{de} (the average electron velocity parallel to **B**) is $4.0c_A$ and the thermal speed v_{te} is $2.0c_A$, which marginally exceeds the linear stability threshold. The ion acoustic instability is stable for $T_e \sim T_i$ (4). Very quickly ($t = 0.55\ \Omega_{ci}^{-1}$), z-dependent fluctuations [$\sim\exp(ik_zz)$, where k_z is the wave vector] develop in the electric field E_z (Fig. 2A). The spatial periodicity of these fluctuations is consistent with a cold (zero temperature) fluid model in which the growth rate of the Buneman instability peaks at a wave vector $k_z = \omega_{pe}/v_{de} = 50.0$ (12).

As reconnection proceeds, the electrons are accelerated in the region near the x-line and the resulting electron drift speed greatly exceeds the Buneman instability threshold (Fig. 3A). As a consequence, the turbulence near the x-line in the 3D simulation becomes very strong (movie S1). The short spatial scale fluctuations (Fig. 2A) coalesce in the z direction and break up in the x direction to form three-dimensionally localized regions of depleted electron density (and enhanced ion density) referred to as electron holes (movie S2) or electrostatic solitary waves (13). At $t = 3.4\ \Omega_{ci}^{-1}$ an electron hole is centered around $x = 1$ in the simulation (Fig. 2B), which is the location of the x-line. The amplitude of the electric field of this hole is $3.0\ c_AB_0/c$. In our simulations, this hole and others propagate downward in the direction of the electron drift (movie S2) at a velocity of around $3c_A$. Because the drift velocity of the electrons is now highest around the x-line and along the separatrices (Fig. 1B), the holes are distributed in these regions. The holes have a

lifetime that is typically comparable to the traversal time of the hole through the periodicity length of the simulation in the z direction. The holes therefore form, grow in time, and then self-destruct. The generation of the electron holes during reconnection is distinct from earlier studies, in which electron holes arose from turbulence driven by counterstreaming electron beams (14, 15) or upstream from shocks (16).

The development of electron holes leads to strong electron scattering and heating in the direction parallel to the magnetic field. At $t = 3.5\ \Omega_{ci}^{-1}$ in the 3D simulations the electron drift velocity near the x-line has approached $10c_A$, consistent with the 2D simulations, but a long tail has formed on the electron velocity distribution, which extends beyond the ion drift speed (Fig. 3B). The scattering of electrons can be represented as an effective drag between the electrons and ions that limits the electron acceleration by the reconnection electric field E_z, which de-

velops during reconnection. This drag can be calculated from the electron momentum equation by averaging over the turbulence. In particular, we average the momentum equation over z to obtain an equation for the z component of the average electron momentum density $\overline{p_{ez}}$,

$$\frac{\partial \overline{p_{ez}}}{\partial t} + \nabla \cdot \overline{\mathbf{v}_e p_{ez}} = -e\overline{n_e}\ \overline{E_z} - e\overline{\tilde{n}_e\tilde{E}_z}$$
$$- \frac{e}{m_ec}(\overline{\mathbf{p}_e} \times \overline{\mathbf{B}})_z \quad (2)$$

where for any A we define $\overline{A}$ as the average of A over z and we have retained only electrostatic fluctuations. The dominant anomalous drag between electrons and ions arises from the correlation of the fluctuations of the electron density and parallel electric field, $D_z = -\overline{\tilde{n}_e\tilde{E}_z}$ (4). In order for the drag to compete with the reconnection electric field $\overline{E_z}$, we require $D_z \sim n_0\overline{E_z}$. At $t = 4.15\ \Omega_{ci}^{-1}$ in the 3D simulations the anomalous drag is spreading
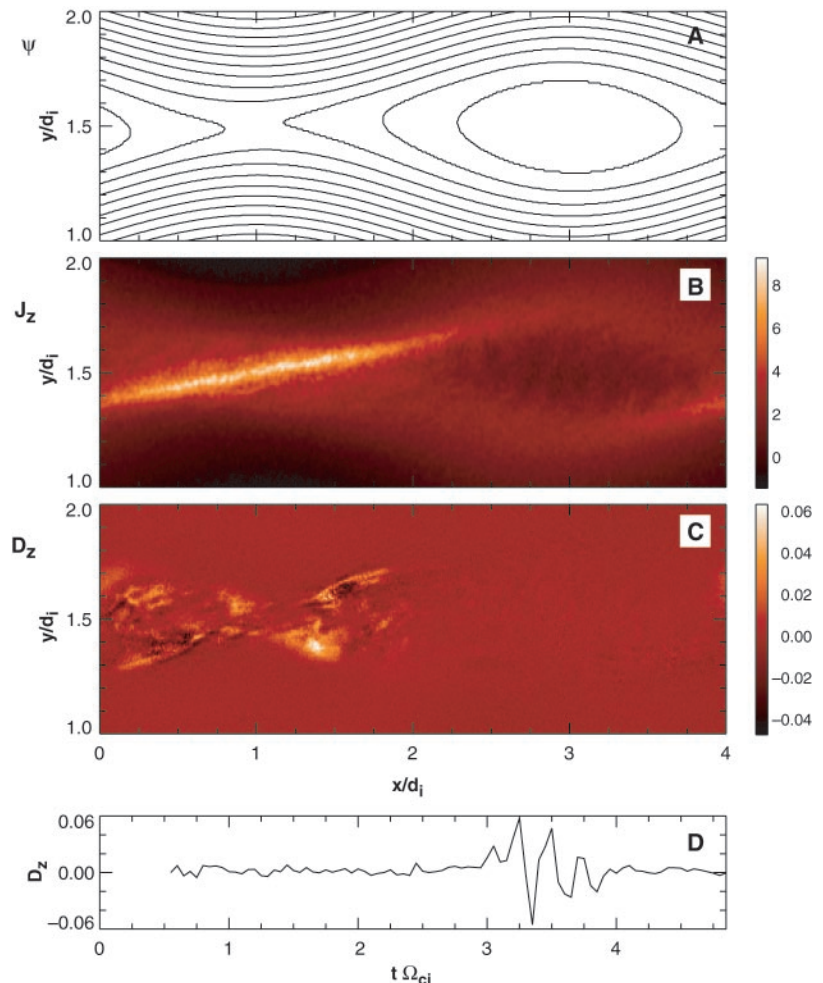
Fig. 1. From the 3D simulation, (**A**) magnetic field lines (averaged over z) and (**B**) current density J_z (normalized to $cB_0/4\pi d_i$) in the x-y plane at $t = 3.4\ \Omega_{ci}^{-1}$. (**C** and **D**) The anomalous drag D_z (normalized to $n_0c_AB_0/c$) is shown at $t = 4.15\ \Omega_{ci}^{-1}$ in (C) and as a function of time at the x-line in (D). In (C) the patchiness of D_z, with positive and negative values, is not consistent with theoretical expectations based on quasilinear theory (4). The absence of a strong correlation of D_z with J_z means that the drag cannot be written as an effective anomalous resistivity.

from the region around the x-line along the separatrices, following the region of high current (Fig. 1C) (movie S1). The reconnection electric field near the x-line is in the positive z direction and is around 0.05 $c_A B_0/c$, so the drag must be positive to balance the driving electric field. The magnitude of the drag is sufficiently large. However, unlike in previous predictions of anomalous resistivity based on quasilinear theory (4), the drag is in no sense smooth. Indeed, the drag is negative in some spatial locations (Fig. 1C) and at these locations adds to the local electric field. The regions of large negative drag correlate with the self-destruction of the electron holes. Given the spatial patchiness of the drag, it is not surprising that at a given spatial location the drag exhibits temporal fluctuations. The time series of the drag at the x-line (Fig. 1D) has a distinct oscillatory behavior with a frequency $\omega \sim \omega_{pi} \sim 20\Omega_{ci}$, which is the lower hybrid frequency, $\omega_{lh} \equiv \omega_{pi}/(1 + \omega_{pe}^2/\Omega_{ce}^2)^{1/2}$

for the parameters of the simulation. The absence of a strong correlation between the drag (Fig. 1C) and the electron current (Fig. 1B) implies that the canonical characterization of the drag as an anomalous resistivity is not valid.

The structure of the electron holes seen in the simulations (Fig. 2B) can be partially understood from the linear dispersion relation of current-driven instabilities in a magnetized plasma. At the early stages of the development of the Buneman instability (Fig. 2A), the structures are extended in the x direction. These extended structures begin to break up as a result of the growth of modes with $k_x \neq 0$. Because of the short scale length and therefore high frequency of these disturbances, the ions respond to the wave fields as if they were unmagnetized. In this limit the dispersion relation for a mode of wave vector **k** at an angle θ with respect to the magnetic field direction z is given by

$$1 - \frac{\omega_{pi}^2}{\omega^2} - \sin^2\theta \frac{\omega_{pe}^2}{(\omega - k_z v_{de})^2 - \Omega_{ce}^2}$$
$$- \cos^2\theta \frac{\omega_{pe}^2}{(\omega - k_z v_{de})^2} = 0 \quad (3)$$

(17), where we have taken the cold plasma limit, $k_x = k \sin\theta$, $k_z = k \cos\theta$, and Ω_{ce} is the electron cyclotron frequency based on the magnetic field B_z. This equation can be solved to obtain the conventional Buneman instability (12) with $\theta = 0$ as well as off-angle modes satisfying $1 \gg \cos\theta > (m_e/m_i)^{1/2}$ by taking $\omega_{pi}/\omega_{pe} = (m_e/m_i)^{1/2}$ as small. To lowest order, Eq. 3 constrains the magnitude of **k**,

$$k = k_0 \equiv \delta\omega_{pe}/v_{de} \quad (4)$$

where $\delta^2 = (1 + \sin^2\theta \, \omega_{pe}^2/\Omega_{ce}^2)^{-1}$. Equation 4 dictates that in the strong magnetic field limit, $\omega_{pe} \ll \Omega_{ce}$, the spectrum of unstable waves will have the same wave vector, k_0, irrespective of whether **k** is parallel or nearly perpendicular to the magnetic field. This is consistent with the electron holes in the simulation (for which $\Omega_{ce}/\omega_{pe} = 2.5$) having the same scale length along and transverse to the field. The growth rate of the instability follows by retaining the term proportional to ω_{pi}^2 as well as finite frequency corrections to the electron parallel response (fourth term). The complex frequency is

$$\omega = (m_e \cos\theta/2m_i)^{1/3} \, \delta\omega_{pe} \, \exp(i\pi/3) \quad (5)$$
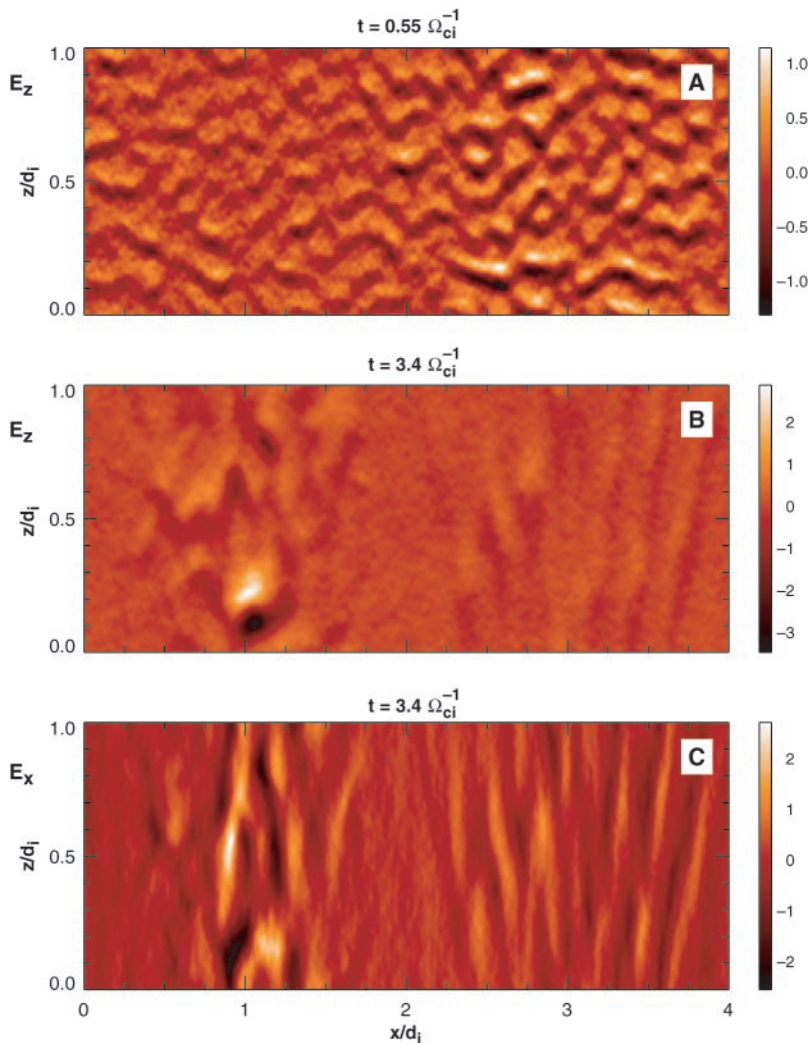
Fig. 2. Parallel electric field perturbations $\tilde{E}_z = E_z - \bar{E}_z$ (normalized to $c_A B_0/c$) in the x-z plane at (**A**) $t = 0.55 \, \Omega_{ci}^{-1}$ and (**B**) $t = 3.4 \, \Omega_{ci}^{-1}$. $\bar{E}_z$ denotes an average of E_z over the z direction. Note the bipolar electric field structure centered around $(x, z) = (1.0, 0.2) \, d_i$ corresponding to an electron hole. (**C**) The transverse field E_x, also at $t = 3.4 \, \Omega_{ci}^{-1}$, is much more extended in z.
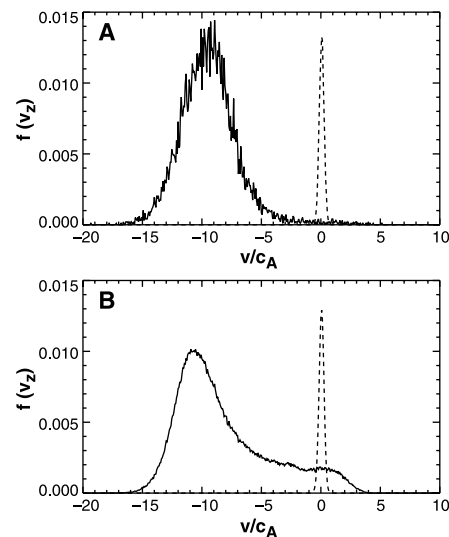
Fig. 3. Parallel ion (dashed line) and electron (solid line) velocity distribution functions $f(v_z)$ around the x-line from (**A**) the 2D simulation at $t = 3.75 \, \Omega_{ci}^{-1}$ and (**B**) the 3D simulation at $t = 3.5 \, \Omega_{ci}^{-1}$. The ion distribution function is reduced by a factor of 10 so the details of the electrons can be seen. In (A) the mean electron drift velocity is $v_{de} \approx 10c_A$, which is far above the Buneman threshold. Note the long tail on the electron distribution function in (B), which is a consequence of the effective drag arising from electron scattering off of the electron holes.

Modes with $\theta \neq 0$ have substantial growth rates. This broad spectrum of waves produces the long tail on the electron velocity distribution (Fig. 3B).

A second important issue concerns the electron hole lifetime and the mechanism responsible for limiting hole electric fields. Two-dimensional simulations in the y-z plane yield amplitudes that are roughly a factor of 3 larger than those in the 3D simulations. The saturation of the 2D system also yields stronger electron scattering than the full 3D system with amplitudes consistent with trapping and reflection of the drifting electrons,

$$e\phi \sim m_e v_{de}^2 / 2 \qquad (6)$$

The saturation in the 3D simulations is linked to the growth of the large transverse electric field E_x (Fig. 2C). This field is substantially more extended along the magnetic field than E_z and takes the form of a wake, which moves with the hole in the negative z direction. The electron hole couples to a lower hybrid wave whose parallel phase speed (z direction) matches that of the hole and whose transverse group velocity is zero. This lower hybrid wave is also a part of the linearly unstable spectrum governed by Eq. 3 but in the limit of nearly perpendicular propagation, $\cos \theta < (m_e/m_i)^{1/2}$. The instability is a resonance between the lower hybrid mode with $\omega \sim \omega_{lh}$ and the electron beam $\omega \sim k_z v_{de}$ and has a growth rate of the order ω_{lh} (4). The amplitude of the wake increases until E_x is sufficiently large to trap the ions, which disrupts the hole. This occurs just after $t = 3.5$ Ω_{ci}^{-1} in the simulation (Fig. 2, B and C). The ion trapping condition yields an upper limit on the associated potential ϕ given by

$$e\phi \sim m_e(v_{de}c_{se}^3)^{1/2} \qquad (7)$$

where $c_{se} = (T_i/m_e)^{1/2}$ is the electron sound velocity. This potential matches the potential of the holes in the 3D simulation at saturation. For $c_{se} < v_{de}$ this expression should replace Eq. 6 as an estimate of the amplitude of electron holes. Although the full dynamics of the coupling of electron holes and lower hybrid waves is not yet fully understood, it appears that the parallel spacing (along **B**) of the electron holes is controlled by the parallel structure of the lower hybrid wave. Further, the time signature of the drag at the x-line (Fig. 1D) suggests that this coupling also controls electron scattering near the x-line.

The holes seen in the 3D numerical simulations initially form in the vicinity of the x-line and later spread along the full length of the magnetic separatrices. Thus, electron holes should be observable both in the vicinity of the x-line and at the edges of the boundary layers that develop as a consequence of reconnection. Observations of holes at boundary layers should dominate the data because of the much larger spatial volume of these regions: The x-line is localized in two spatial directions while boundary layers are localized in one direction. The satellite observations in the magnetosphere are consistent with this expectation. Electron holes are seen in the magnetotail at the interface between the dense plasma sheet and the lobe (18–20), in the high-latitude cusp (20) and the magnetopause current layer (21). All of these regions are associated with boundary layers whose formation is linked to magnetic reconnection.

We have compared data taken from the Polar spacecraft at Earth's magnetopause with our simulations and theory. Large-amplitude electric field waveforms with electron holes were measured during six complete crossings of the magnetopause and during eight partial crossings (the satellite entered and exited the same side of the magnetopause). All of the observations of electron holes by the Polar satellite occurred within the magnetopause current layer (Fig. 4A), specifically the magnetospheric edge of the current layer. The present 3D simulations did not include the asymmetry in the density and magnetic field across the magnetopause and therefore could not distinguish the two sides of the current layer. However, in 2D reconnection simulations that include these asymmetries, the electron drift velocity v_{de} on the magnetosphere side greatly exceeds that on the magnetosheath side because of the high magnetic field gradient and lower plasma density ($v_{de} \sim J_z/n_e$) at this location (22). Thus, the locations of electron holes seen in the data are consistent with the theoretical expectations.

For a more detailed comparison with the simulations, we show the time series of the parallel electric field as measured by the Polar
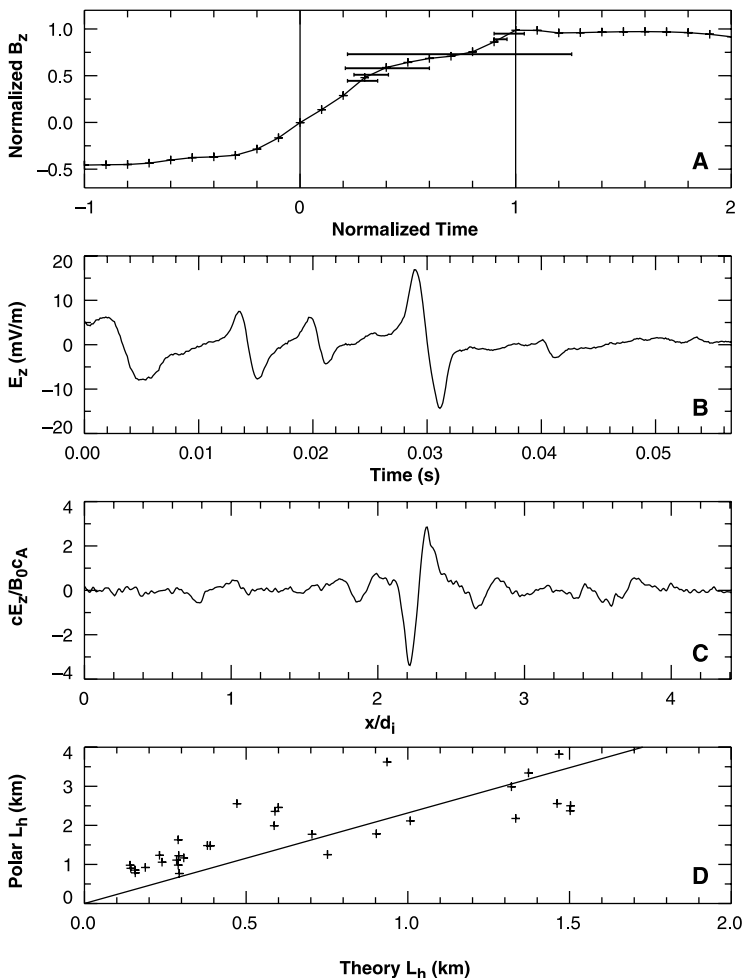
Fig. 4. (A) Location of strong electric field activity (horizontal bars) in six Polar spacecraft magnetopause crossings plotted against the normalized magnetic field data. To construct the normalized field, we normalized the value of B_z for each crossing (B_x in simulation coordinates) by the value in the magnetosphere. The time when the satellite encountered the magnetospheric side of the current sheet was defined as $t = 1$, and the zero crossing of B_z was defined as $t = 0$. These two markers provided the temporal normalization for each crossing. The normalized fields from all six crossings were then averaged. **(B and C)** Parallel electric field signatures as seen in the Polar magnetopause data (B) and along a trajectory through the electron hole in Fig. 2B (C). **(D)** Hole widths L_h as measured by Polar versus the theoretical prediction $L_h \sim 2\pi(v_h/\omega_{pe})(m_i/m_e)^{1/3}$. The near-linear relationship (solid line) indicates a good correlation between theory and experiment although the slope is less than unity, indicating that the theory prediction of electron hole scale lengths is too small by a factor of 2.

spacecraft on 31 March 2002 starting at 15:58:14.245 at a distance of $8.85R_e$ (with R_e the radius of Earth) and at 11.18 magnetic local time (MLT) (Fig. 4B). The localized bipolar parallel electric field is consistent with previously published satellite data (*18–21*). To model the parallel electric field that might be seen by a satellite crossing the magnetopause as a result of the rapid convection of electron holes, we plot E_z obtained along a trajectory in the x-z plane through the hole in our simulation (Fig. 2B) at an angle of 10° with respect to the z axis. The strongly localized bipolar parallel electric field is consistent with the Polar data. Note, however, that the parity of the holes in the data is inverted compared with the simulation. The parity depends on the direction of the electron hole velocity compared with the direction of the ambient magnetic field. Both parities are seen in the spacecraft data.

The comparison with satellite data is complicated by the fact that the simulations cannot at the present time be carried out with realistic electron to ion mass ratios. Also, the simulations presented have $\omega_{pe} < \Omega_{ce}$ while at the magnetopause the inequality is reversed. The simulations therefore have to be extrapolated to the magnetopause using the theoretical scaling of the size of the electron hole, $L_h \sim 2\pi v_{de}/\omega_{pe}$, its velocity $v_h \sim (m_e/m_i)^{1/3} v_{de}$, and the maximum potential ϕ_h, given by the smaller of the expressions in Eqs. 6 and 7. The primary uncertainty in comparing with the satellite data concerns the electron streaming velocity. The sweep time to measure the electron velocity distribution on Polar is around 4 s, whereas trains of electron holes typically last 0.1 s or less and single holes transit in 10^{-3} s. The combination of the wave train duration and the typical relative drift speed of 10 km/s between the magnetopause and spacecraft implies that electron holes are localized to regions of transverse (to the magnetopause) scale around 1 km, which is roughly the electron skin depth c/ω_{pe} and is consistent with the simulations. Because such narrow electron beams are not measurable with Polar, it is not possible to correlate beam parameters with electron hole velocities. In the absence of adequate data on the electron drift speed, we can check the self-consistency of the measured hole velocity and scale length by eliminating the electron drift speed, which yields the relation $L_h \sim 2\pi(v_h/\omega_{pe})(m_i/m_e)^{1/3}$. The plasma density during the time interval in Fig. 4B is around 4/cm³ (based on the measurement of the spacecraft potential) and the measured hole velocity is 260 km/s. The predicted hole scale length is therefore around 0.7 km compared with the measured value of 1.4 km. This relationship has also been tested on the basis of five magnetopause crossings where high–time resolution electric field and electron density moment data from Polar are available. The hole velocities in this data set have a range $v_h \sim 250$ to 2000 km/s. The predicted hole size scaling agrees well with

Polar data (Fig. 4D). The measured hole potentials in this same data set range from 0.1 to 10 V. Comparison with theory is again complicated by the absence of resolved data on the electron streaming velocity. Taking $v_{de} \sim (m_i/m_e)^{1/3} v_h \sim$ 3200 km/s for the observed hole (Fig. 4B), we estimate $e\phi \sim m_e v_{de}^2/2 \sim 30$ eV, compared with $e\phi \sim 10$ eV from the Polar data. On the other hand, for $T_e \sim 50$ eV, $v_{te} \sim 2800$ km/s, hence a drift speed of 3200 km/s is close to marginal stability of the Buneman instability.

Consistent with the 3D simulations, strong lower hybrid waves are typically measured in satellite crossings of the magnetopause where bursts of electron holes are observed. In satellite observations of electron holes in the auroral ionosphere, waves in the lower hybrid range of frequencies are also observed (*23*). However, the coupling of these distinct classes of wave fields in the satellite data has not yet been explored. The inverse problem, driving electron parallel current with lower hybrid waves, has been explored for many years in laboratory fusion experiments (*24*). Thus, the role of such waves as a mechanism for retarding current should not be surprising.

References and Notes

1. E. N. Parker, *J. Geophys. Res.* **62**, 509 (1957).
2. P. A. Sweet, in *Electromagnetic Phenomena in Cosmical Physics*, B. Lehnert, Ed. (Cambridge Univ. Press, New York, 1958), p. 123.
3. D. Biskamp, *Phys. Fluids* **29**, 1520 (1986).
4. A. A. Galeev, R. Z. Sagdeev, *Handbook of Plasma Physics* (North-Holland Physics, Amsterdam, 1984), vol. 2, chap. 6.1, p. 271.
5. H. E. Petschek, in *AAS/NASA Symposium on the Phys-ics of Solar Flares*, W. N. Ness, Ed. (NASA, Washington, DC, 1964), p. 425.
6. T. Sato, T. Hayashi, *Phys. Fluids* **22**, 1189 (1979).
7. R. P. Lin, H. S. Hudson, *Sol. Phys.* **17**, 412 (1971).
8. M. Oieroset, R. P. Lin, T. D. Phan, D. E. Larson, S. D. Bale, *Phys. Rev. Lett.* **89**, 195001 (2002).
9. M. Temerin, K. Cerny, W. Lotko, F. S. Mozer, *Phys. Rev. Lett.* **48**, 1175 (1982).
10. F. Mozer, R. Ergun, M. Temerin, C. Cattell, *Phys. Rev. Lett.* **79**, 1281 (1997).
11. A. Zeiler *et al.*, *J. Geophys. Res.* **107**, 1230 (2002).
12. O. Buneman, *Phys. Rev.* **115**, 503 (1959).
13. S. Bujarbarua, H. Schamel, *J. Plasma Phys.* **25**, 515 (1981).
14. Y. Omura, H. Matsumoto, T. Miyake, H. Kojima, *J. Geophys. Res.* **101**, 2685 (1996).
15. D. L. Newman, M. V. Goldman, R. E. Ergun, A. Mangeney, *Phys. Rev. Lett.* **87**, 255001 (2001).
16. N. Shimada, M. Hoshino, *Astrophys. J.* **543**, L67 (2000).
17. A. B. Mikhailovskii, *Theory of Plasma Instabilities, Vol. 1* (Consultants Bureau, New York, 1974).
18. J. Franz, P. Kintner, J. Pickett, *Geophys. Res. Lett.* **25**, 1277 (1998).
19. H. Matsumoto, L. A. Frank, Y. Omura, H. Kojima, *Geophys. Res. Lett.* **26**, 421 (1999).
20. C. Cattell, J. Dombeck, J. R. Wygant, M. K. Hudson, *Geophys. Res. Lett.* **26**, 425 (1999).
21. C. Cattell, J. Crumley, J. Dombeck, J. Wygant, F. S. Mozer, *Geophys. Res. Lett.* **29** (no. 5), 9-1 (2002).
22. M. Swisdak, B. N. Rogers, J. F. Drake, M. A. Shay, *J. Geophys. Res.*, in press.
23. R. Pottelette, R. Treumann, M. Berthomier, *J. Geophys. Res.* **106**, 8465 (2001).
24. M. Porkolab, R. P. H. Chang, *Rev. Mod. Phys.* **50**, 745 (1978).
25. Supported in part by the U.S. Department of Energy, NASA, and NSF. We thank M. Porkolab for helpful discussions on the structure on the lower hybrid wave.

Eocene El Niño: Evidence for Robust Tropical Dynamics in the "Hothouse"

Matthew Huber*† and Rodrigo Caballero

Much uncertainty surrounds the interactions between the El Niño–Southern Oscillation (ENSO) and long-term global change. Past periods of extreme global warmth, exemplified by the Eocene (55 to 35 million years ago), provide a good testing ground for theories for this interaction. Here, we compare Eocene coupled climate model simulations with annually resolved variability records preserved in lake sediments. The simulations show Pacific deep-ocean and high-latitude surface warming of ~10°C but little change in the tropical thermocline structure, atmosphere-ocean dynamics, and ENSO, in agreement with proxies. This result contrasts with theories linking past and future "hothouse" climates with a shift toward a permanent El Niño–like state.

Whereas ENSO's interannual impact on the global climate and the carbon cycle is well established (*1–3*), the role of the tropical Pacific in long–time-scale climate change remains controversial (*4, 5*). The Pacific ocean-atmosphere system is governed by a delicate balance of dynamical feedbacks (*6–8*), rais-

ing concern about its stability to external forcing. Conceivably, the region's climate could undergo major, long-term reorganizations (*9*), which could strongly modulate global change. In particular, theory indicates that any changes acting to weaken the "Bjerknes" feedback—the instability at the